Learning chemical potentials and parameters from voltage data for multi-phase battery modeling

N.B. When citing this work, cite the original published paper.

(article starts on next page)

Learning chemical potentials and parameters from voltage data for multi-phase battery modeling

Yicun Huang[a], Torsten Wik[a], Donal P. Finegan[b], Yang Li[a], Changfu Zou[a,*]

[a]*Department of Electrical Engineering, Chalmers University of Technology, Gothenburg, 412 96, Sweden.*

[b]*National Renewable Energy Laboratory, 15013 Denver West Parkway, Golden, CO 80401, USA.*

Abstract

Phase transition is a crucial phenomenon in many battery chemistries, especially for lithium-ion cells based on graphite electrodes. Accurately modeling this phenomenon is important for predicting and optimizing the performance of batteries. Traditional approaches rely on the first-principle derivation of the chemical potential or, more simply, adopt open-circuit potential (OCP) data, often present limited predictive accuracy, and fail to capture the complex free-energy barriers and multi-phase intercalation dynamics. In this work, we introduce a physics-based learning framework, termed Bayesian model-integrated neural networks (BMINN), that infers electrode-specific chemical potentials and Gibbs free energies directly from current-voltage data, without relying on restrictive assumptions about their functional forms. By integrating physics-based equations with Bayesian neural networks, our method uncovers hidden physics while quantifying uncertainties, enabling enhanced robustness and accurate modeling of chemical potentials. Validated by experimental results, the proposed physics-based learning approach outperforms conventional OCP-fitted and porous electrode theory (PET)-based chemical potential models. It successfully captures critical features such as staging structures and energy barriers that govern battery dynamics and phase transitions. Furthermore, we illustrate the utility of accurate chemical potentials in *operando* X-ray diffraction (XRD) spectra, which provides deeper insights into the dynamics of lithium intercalation in graphite electrodes.

---

*Corresponding author. Address: Hörsalsvägen 11, SE-412 96 Gothenburg, Sweden.
Email address: changfu.zou@chalmers.se (Changfu Zou)

Graphical Abstract
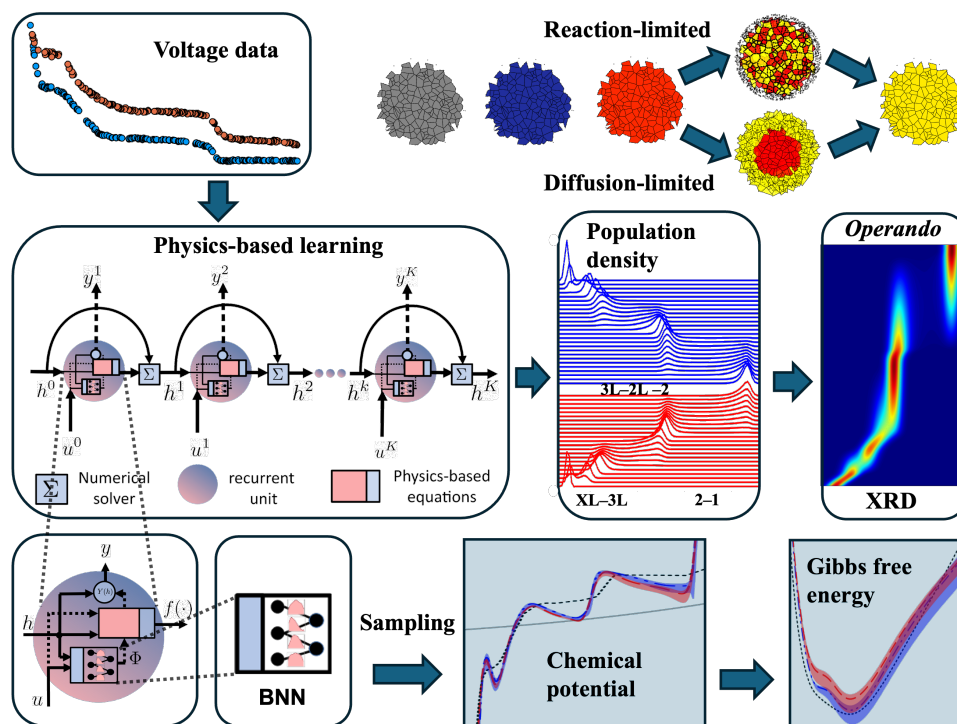
1. Introduction

Next-generation porous electrodes for high-rate and high-capacity batteries demand fast ion transport across the electrode lattice sites, within the electrolyte, and at interfaces. For decades, graphite has been the preferred material in lithium-ion batteries due to its low cost and the relatively small volume change compared to alternatives such as silicon. As a two-dimensional (2D) intercalation material, graphite is available in various microparticulate forms, such as spherical and flake-like graphite particles [1]. At low C-rates, a graphite electrode undergoes phase transitions between at least four phases, reflected by three prominent open-circuit potential (OCP) plateaus [2]. At high C-rates, however, particle filling is limited by solid-state diffusion in each phase and phase boundary migrations, different from non-phase-separating compounds, such as nickel-manganese-cobalt (NMC) and other solid-solution-based electrode materials [3–5]. This solid-state transport limitation of graphite electrodes cannot be fully described by classical intercalation models, such as shrinking core-type models that assume phase equilibrium at the interfaces and solid-solution elsewhere [6].

Physically, the transport limitation of lithium ions is attributed to sequential events during graphite lithiation, com-

monly referred to as the stages of graphite intercalation. These stages are conventionally named based on the average number of graphene layers between each lithium layer. For a given average number, the lithium-graphene crystallographic structure is open to two distinct interpretations, known as the Rüdorff-Hoffman [7] and Daumas-Hérold [8] staging structures. Thermodynamically, these stages correspond to minima in the Gibbs free energy, while the intermediate regions align with miscibility gaps in the chemical potential. Within these miscibility gaps, phase transitions occur between coexisting phases as the system seeks to minimize its free energy. The dynamics of these phase transitions in graphite electrodes are governed by the driving overpotential. To predict the intercalation dynamics during phase separation and reliably track the mass fraction of, e.g., Stage 1, where parasitic lithium plating is likely to occur, accurate models of Gibbs free energy and chemical potential are required. In particular, the height of free-energy barriers plays a critical role, as experimental evidence indicates that certain phase transitions in graphite electrodes can lag behind others under specific intercalation rates [9].

The Gibbs free energy is derived from the sum of the products of the chemical potentials of the intercalating layers and their corresponding ion concentrations. For two-phase materials, such as lithium iron phosphate, this energy can be effectively modeled using a 1D double-well function [10, 11]. In contrast, for multi-phase materials like graphite, a multi-dimensional free energy functional is required to account for the presence of different staging structures. Smith *et al.* [12] proposed a 2D free energy model that is consistent with the Rüdorff-Hoffman bilayer structure. This model incorporates two 1D regular-solution free energies representing two alternating lithium layers and captures only the Stage 2–1 transition. Chandesris *et al.* [13, 14] extended this approach by incorporating the short-range periodicity of the Daumas-Hérold structure, which enables the description of additional phases and transitions.

While these free energy models effectively capture the major voltage plateaus for single-crystal graphite particles, their applicability to realistic graphite ensembles in electrodes remains uncertain. Electrode-level simulations based on them typically consider volume-averaged or coarse-grained particles, which fail to fully capture intercalation behaviors of the electrode. In contrast, graphite electrodes in commercial cells consist of polycrystalline graphite particles with hierarchical microstructures, varying in size and defect [1]. To achieve high predictive accuracy of electrode-level simulations, it is essential to develop electrode-specific chemical potential models that can be directly learned from external voltage measurements, without relying on predefined, unreliable functional forms. Such models are crucial for capturing the complex multi-phase intercalation dynamics in graphite electrodes.

In this work, we present a framework to learn electrode-specific chemical potential models, addressing key limitations in the modeling of multi-phase intercalation dynamics in polycrystalline graphite electrodes. Using physics-based

3

learning applied to two distinct formulations grounded in first principles, our approach incorporates domain-specific knowledge directly into the deep-learning framework. This results in chemical potential and Gibbs free energy models capable of identifying transient phases and multi-phase intercalation dynamics including population density and phase separation behaviors.

An important feature of our approach exists in its ability to capture free-energy barriers, which are critical for understanding lagging phase transitions at high intercalation rates. Furthermore, we will show that the proposed models can accurately reproduce experimentally challenging *operando* X-ray diffraction (XRD) spectra, which thereby overcomes the high costs and specialized requirements of *operando* XRD setups. By enabling direct, data-driven learning of chemical potential models from external voltage measurements, our framework eliminates the need for computationally expensive simulations of individual single-crystal particles and costly *operando* XRD experiments.
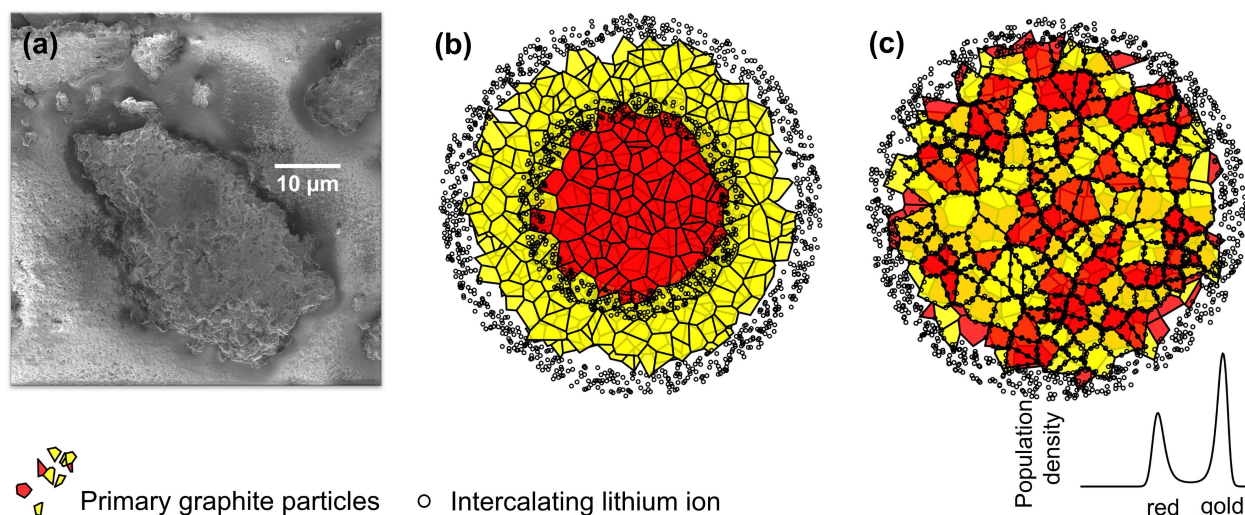

Figure 1: Hierarchical microstructure of a graphite particle. (a) SEM image of a secondary polycrystalline particle of synthetic graphite. (b) A diffusion-limited picture for the secondary polycrystalline particle. (c) A reaction-limited picture of the primary, single-crystalline particles. During phase transitions, the ensemble of primary particles separates into two phases; for example, a Stage 2–1 transition is characterized by a bimodal population density with two peaks centered around the red phase and gold phase. Experimentally, both phase morphologies have been observed in a graphite electrode [15] under the same operational condition, implying that both diffusion-limited and reaction-limited physical pictures are plausible.

Physical picture

To model electrode-specific chemical potential through physics-based learning, it is essential to establish the intercalation mechanism. However, there is ongoing debate regarding how lithium ions intercalate into graphite electrodes. Traditionally, lithium intercalation has been considered diffusion-limited under typical battery operating conditions. This perspective is based on the core-shell phase separations commonly observed in graphite electrodes [15, 16].

4

The extent of diffusion limitation is influenced by various factors, including C-rate, particle size, geometry, surface morphology, and electrode thickness. Fig. 1a presents a scanning electron microscopy (SEM) image of a secondary polycrystalline particle composed of tens of thousands of primary single-crystal particles. The ion intercalation of these densely packed primary particles within the secondary structure can be modeled using both diffusion-limited and reaction-limited assumptions.

First, for a diffusion-limited picture depicted in Fig. 1b, we utilize a phase-field formulation [17] adapted to describe particle filling limited by solid-state transport within a secondary particle, governed by chemical potential. In addition, phase transitions are not confined solely to diffusion-limited secondary particles but also occur at the scale of a primary particle ensemble. These ensemble-scale phase transitions are driven by interfacial reactions [18, 19], which are determined by chemical potential differences [20, 21]. Second, a scaling law predicts that when the average particle size is below one micron and with applied current less than 100C for graphite, the system becomes reaction-limited [22]. Considering submicron-sized primary particles commonly found under typical operating conditions [1], we adopt a reaction-limited formulation [21, 23] for primary particle intercalation, as illustrated in Fig. 1c. While diffusion-limited and reaction-limited pictures can co-exist and are observed in graphite electrodes under the same conditions [15], we consider both in our physics-based learning framework for modeling chemical potential.

Physics-based learning

Physics-based learning is a hybrid modeling approach that combines domain-specific knowledge from classical partial differential equation (PDE)-based systems with data-driven techniques [24]. This methodology has been previously utilized for model order reduction to accelerate battery model simulations [25]. To enable the efficient learning of chemical potentials, we extend this method to uncover hidden physics and address uncertainties by incorporating the Bayesian inference, leading to Bayesian model integrated neural networks (BMINN). The major innovation of BMINN is its capability to accurately infer chemical potentials from voltage data alone. This is particularly critical for multi-phase battery modeling, where precise chemical potential profiles are essential to capturing phase transition dynamics in graphite electrodes.

BMINN achieves this by parameterizing hidden physics using a flexible and stochastic function that can relate to any signal in a physics-based model, including time, differential states, algebraic states, control inputs, and spatial coordinates. Unlike methods such as the SINDy algorithm [26], BMINN does not impose predefined functional forms for unknown physics. Compared to inverse physics-informed neural networks (iPINNs) [27], which rely on learning spe-

cific solution trajectories in the inverse problem (*Supporting Information S8*), BMINN is designed to uncover hidden system dynamics while providing uncertainty quantification, as mentioned earlier. The hybrid framework combines known physics-based equations with Bayesian neural networks to produce a data-driven function that accounts for both parameterization errors and modeling errors resulting from model mis-specifications. By enabling robust uncertainty quantification and physics-based insights, BMINN provides a versatile and generalizable tool for modeling electrochemical systems.

Results

Chemical potential and Gibbs free energy

Using BMINN and experimentally measured half-cell current-voltage data (*Supporting Information S1*), Gibbs free energies g and chemical potentials μ as functions of the filling fraction, x in Li_xC_6, are learned with uncertainty quantification. These quantities are inferred from data collected during a C/40 charge-discharge cycle at 25 °C, which employs either diffusion-limited or reaction-limited formulation (*Supporting Information S2–S4*). Specifically, porous electrode theory (PET)-based chemical potentials take on a logarithmic form, while OCP-fitted chemical potentials are obtained from OCP measurements. In contrast, all other energies and potentials are inferred without imposing any predefined functional forms. This allows greater flexibility in capturing hidden physics. This flexibility is important, as modeling errors often arise from incorrect assumptions about functional dependencies. By avoiding such constraints, BMINN leverages the universal approximation capabilities of neural networks to identify hidden physics and provide accurate, data-driven insights into multi-phase intercalation dynamics.

In addition to enabling flexible inference, it is important to assess the credibility of the inferred energies and potentials. Point estimates, such as maximum *a-posteriori* (MAP) or maximum likelihood estimation, often fail to account for the credibility or variability of the inferred parameters, which can be particularly problematic when dealing with limited and noisy data. In the absence of internal sensors, external and often noisy current-voltage data make a Bayesian formulation particularly suitable for this purpose. As shown in Fig. 2, posterior distributions of energies and potentials are sampled, revealing that they converge to unimodal distributions. Interestingly, the posterior distributions associated with the phase-field formulation exhibit a wider confidence interval (CI), which indicates a higher level of uncertainty compared to the reaction-limited formulation. This quantification of uncertainty provides valuable insights into factors such as data noise and the influence of the specific physics-based formulation used.
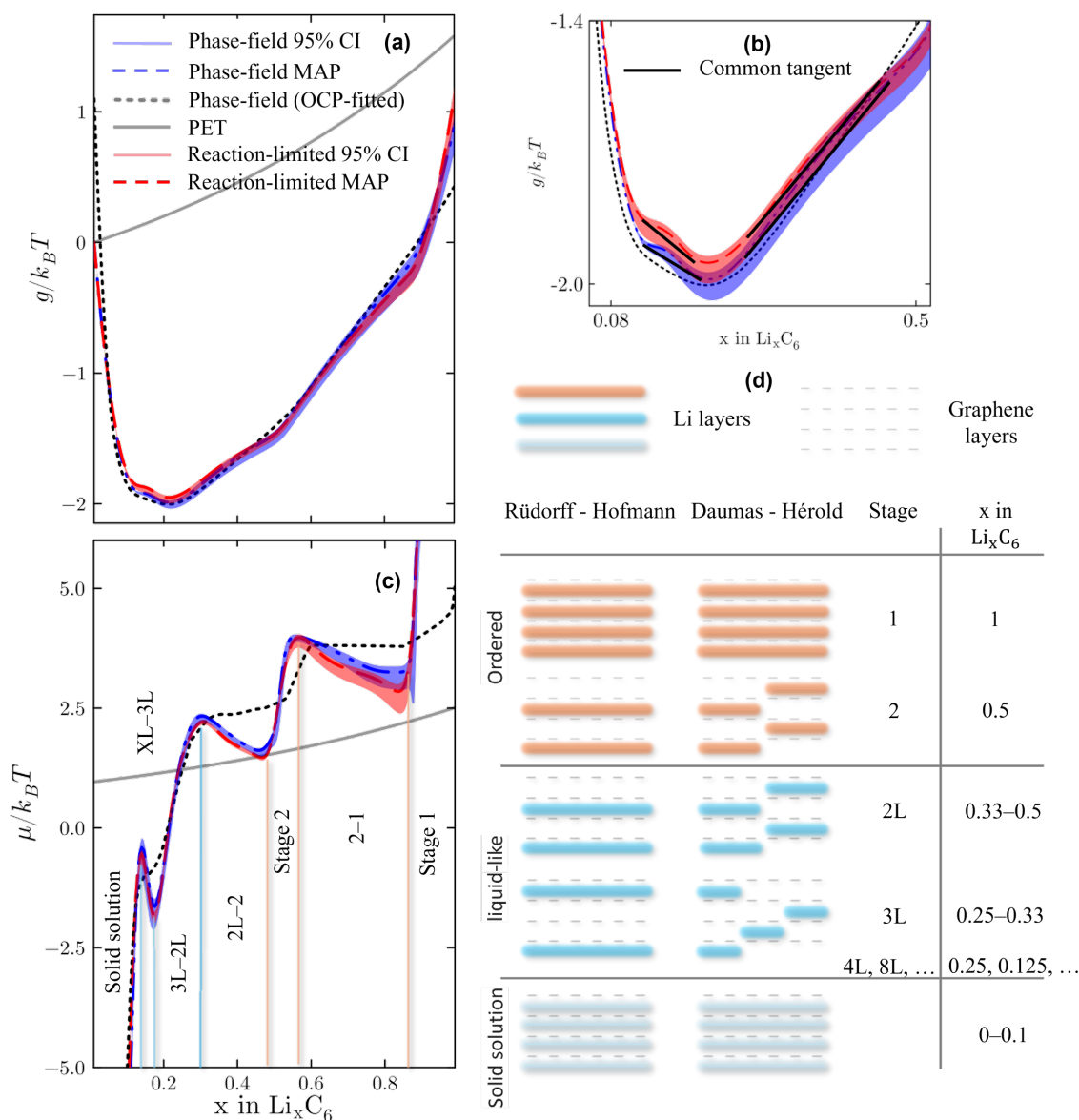
6

Figure 2: (a) Gibbs free energies. (b) Two common tangents (black solid lines) of the maximum *a-posteriori* value (dashed line) of the Gibbs free energies for the 3L–2L and 2L–2 transitions. (c) Chemical potentials. All the energies and potentials are scaled to thermal energy $k_B T$, and are sampled from the posterior distributions obtained from a C/40 charge-discharge cycle. The intensity of the color is proportional to the probability density of the posterior distribution. (d) The staging structures of different stages, including dense stages where the lithium ions are intercalated on interstitial sites and liquid-like stages where graphene layers are filled without particular in-plane order. Disordered lithium ordering with lithium content lower than 3L, e.g. Stage 4L and 8L, are denoted by XL.

As shown in Fig. 2a, the Gibbs free energies learned with phase-field and reaction-limited formulations display four distinct energy wells at filling fractions of approximately 0.1, 0.2, 0.5, and 0.9. These energy wells correspond to Stages 3L, 2L, 2, and 1 of the lithiated graphite phases, respectively. Preceding Stage 3L, we designate XL to represent liquid-like structures that exhibit a periodicity beyond three layers. Compared to a multi-phase-field model [12], which only captures transitions between stable phases, both Gibbs free energy profiles derived from the two physics-

based formulations exhibit energy minima associated with transient liquid-like (L) phases. Thermodynamically, the common tangents of the double-well energies at 3L–2L, 2L–2, and 2–1 coincide with the filling fractions where voltage plateaus are observed. Two of these tangents are illustrated for the maximum *a-posteriori* (MAP) chemical potentials in Fig. 2b.

The staging is clearly identifiable in chemical potentials μ, which represent the change in Gibbs free energies, as shown in Fig. 2c. The notation of the transient phases signifies different stacking structures beyond integer average numbers of graphene layers between lithium layers [6], as illustrated in Fig. 2d. Phase transitions occur between the extrema of the chemical potentials, where $d\mu/dx = 0$. For the experimentally inaccessible concentration regions where x is close to 0 and 1, corresponding to fully de-lithiated and lithiated states, both the Gibbs free energy and chemical potential models become unreliable. However, the particle population adopting these concentrations is negligible, as the cutoff voltages typically prevent the average capacity from reaching these regions. In practice, these regions can be extrapolated using logarithmic functions so that μ approaches $-\infty$ at $x = 0$ and ∞ at $x = 1$ [28], although it may introduce instabilities in the numerical schemes of physics-based simulations. Moreover, the energies and potentials learned using the two physics-based formulations are consistent in their overall shapes but show slight differences in numerical values. For example, the chemical potential learned using a phase-field formulation during a Stage 2–1 transition is lower compared to the chemical potential learned using a reaction-limited formulation. This is expected since the two physics-based formulations are based on different predefined mathematical structures, even though they are trained on the same dataset.

In comparison, OCP-fitted energy and potential curves commonly used in existing electrode-specific phase-field formulations [29–31], as plotted in Fig. 2a and Fig. 2c capture the general trend, but many features are missing. The OCP-fitted chemical potential is derived using the Ernst relation $\mu = e_0(\phi_{OCP} - \phi_{ref})$, where e_0 is the elemental charge, ϕ_{OCP} represents a fitting function of OCP, and ϕ_{ref} is a reference potential taken as the voltage of the first major plateau. As shown in Fig. 2c, the OCP-fitted chemical potential is a monotonic function in which, within the plateau regions, some distinct stages (e.g., XL, 3L, and 2L) are ambiguous to identify. For the OCP-fitted Gibbs free energy in Fig. 2a, the energy barriers are absent, which is not thermodynamically consistent with phase transitions occurring in graphite electrodes. Similarly, classical intercalation models, such as Newman's model based on porous electrode theory [32], assume a chemical potential of the form $\mu = k_B T \ln x$ where k_B and T are the Boltzmann constant and temperature. A monotonic chemical potential does not result in phase coexistence and energy barriers in the Gibbs free energy. These energy barriers not only display plateaus (through common tangent construction) in equilibrium but also play an important role in the intercalation dynamics. It was observed in an *operando* XRD study [9] that lithiation ceases

8

in regions where Stage 2 is reached during charge. In kinetic simulations of realistic graphite electrodes, it is crucial to take into account the energy barriers so that regions undergoing transitions associated with smaller energy barriers draw higher current rates, consistent with experimental observations.
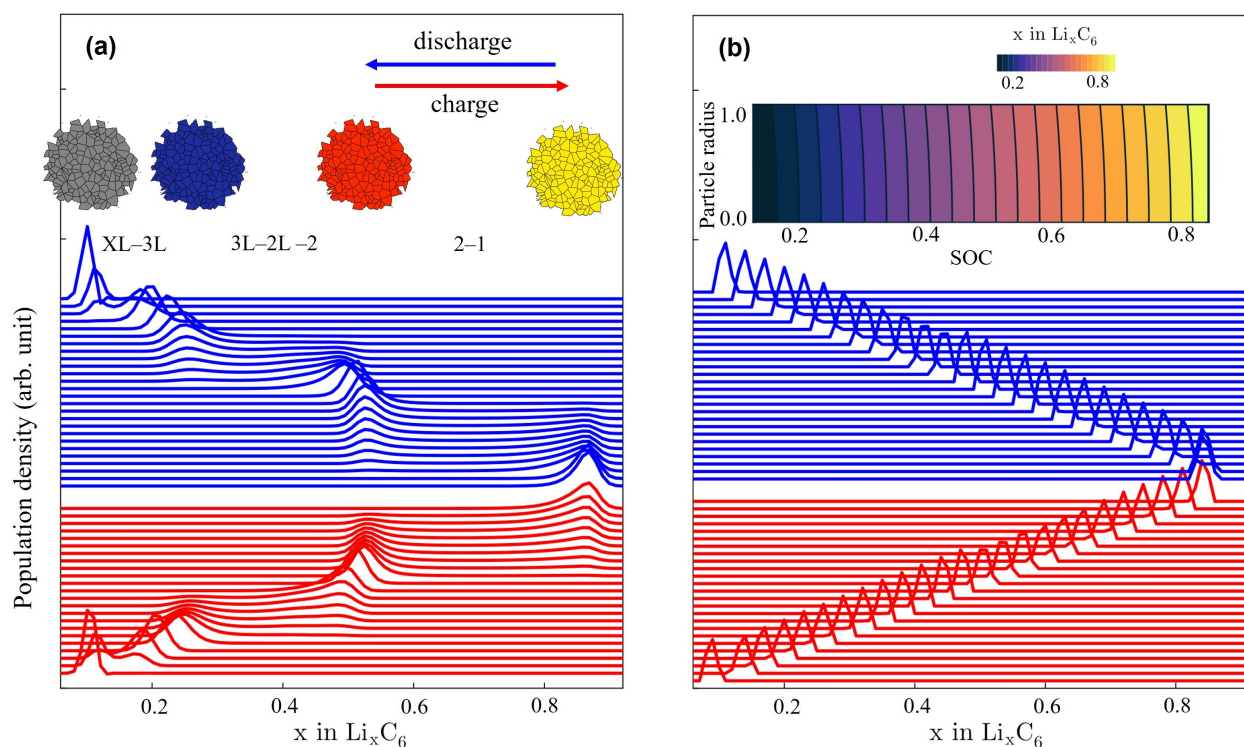

Figure 3: Population densities during a C/20 charge (red) and discharge (blue) cycle resulting from (a) the reaction-limited Gibbs free energy model and (b) the PET-based Gibbs free energy model. Since graphite is a chromogenic material, the color of the particles in the inset of (a) corresponds to those observed in optical experiments [15]. The inset in (b) shows a spatiotemporal plot of the filling fraction for a single (volume-averaged) secondary particle. The population densities for the PET-based model are computed from the spatio-temporal profile of the filling fraction (see *Supporting Information*).

Validation

To further illustrate the importance of a thermodynamically consistent description of Gibbs free energy in graphite intercalation dynamics, we compare different free energy models. In Fig. 3a, the evolution of population densities resulting from the reaction-limited Gibbs free energy model undergoing a C/20 charge-discharge cycle is plotted. The simulation starts with an equilibrium, unimodal distribution at a low state of charge (SOC) value at the beginning of charge. Subsequently, it undergoes three major phase transitions, i.e. XL–3L, 3L–2, and 2–1, each characterized by their corresponding bimodal distributions. Throughout these phase transitions, one peak expands and grows at the expense of the other; for instance, the Stage 1 peak grows while the Stage 2 peak diminishes during the 2–1 transition. The discharge distributions follow a similar mechanism, capturing all phase transitions, but they are not

9

exact reversals of the charge distributions over time due to the combined effects of hysteresis and polarization. In contrast, the population densities resulting from the PET-based model exhibit an advection of a unimodal distribution throughout charge and discharge. As shown in Fig. 3b, there is no expansion, split, or growth of the peak observed. Moreover, no discrepancies between charge and discharge arise from the hysteretic effect, which is not consistent with graphite [33, 34]. It can be concluded that although classical intercalation models may reproduce the voltage behavior of a graphite electrode, they do not accurately model the internal states.

Experimental *in situ* and *operando* techniques probing the internal states of a battery include XRD [9, 35], neutron diffraction [36], and optical microscopy [15, 30]. These methods typically involve unrealistic *operando* cell designs or costly experiments, making them infeasible for periodic assessments of commercial battery cells in the field. However, it is well-known that degradation processes, such as lithium plating, are closely coupled with graphite internal states [37]. Therefore, an accurate model for the internal states of graphite electrodes is highly desirable. To validate different models, the XRD patterns resulting from each model are computed (*Supporting Information*). Fig. 4a shows an *operando* XRD measurement of a graphite electrode undergoing a C/20 charge at 25 °C [35]. The simulated contour plots of changes in the 2θ angle and intensity of graphite basal reflections for various models are shown in the same figure. It can be seen that the simulated *operando* XRD resulting from the phase-field and reaction-limited free energy models closely resemble the overall pattern of experimental measurements, as shown in Fig. 4b and Fig. 4c, respectively. The PET-based free energy model in Fig. 4d produces a solid-solution pattern throughout the charge, which differs significantly from the experiment. Fig. 4e and Fig. 4f show the results of OCP-fitted free energy models in combination with the phase-field and reaction-limited formulations, respectively. These models exhibit solid-solution-like behavior from the start of charging to Stage 2, located at around $25.2°$ in 2θ, differing from the phase separation patterns resulting from our free energy models in Fig. 4b and Fig. 4c and the experiment. Furthermore, the Stage 2–1 transition for the OCP-fitted models, which should initiate at around 50% SOC, is significantly delayed and behaves like a solid solution from 50% to 65% SOC. These behaviors are inconsistent with the experimentally measured XRD pattern.

The above results clearly reveal how important an accurate and realistic description of the Gibbs free energy is in modeling the internal intercalation dynamics of graphite electrodes. Even though the PET-based and OCP-fitted models successfully reproduce current-voltage behaviors of graphite electrodes through system identification [38, 39], the accuracy of these models in the internal states can be erroneous. Our models, based on physics-based Bayesian learning, prescribe accurate Gibbs free energies with realistic energy barriers and chemical potentials. The energy barriers are crucial in the heterogeneous lithiation of graphite under fast-charging conditions. Larger energy barriers inhibit local
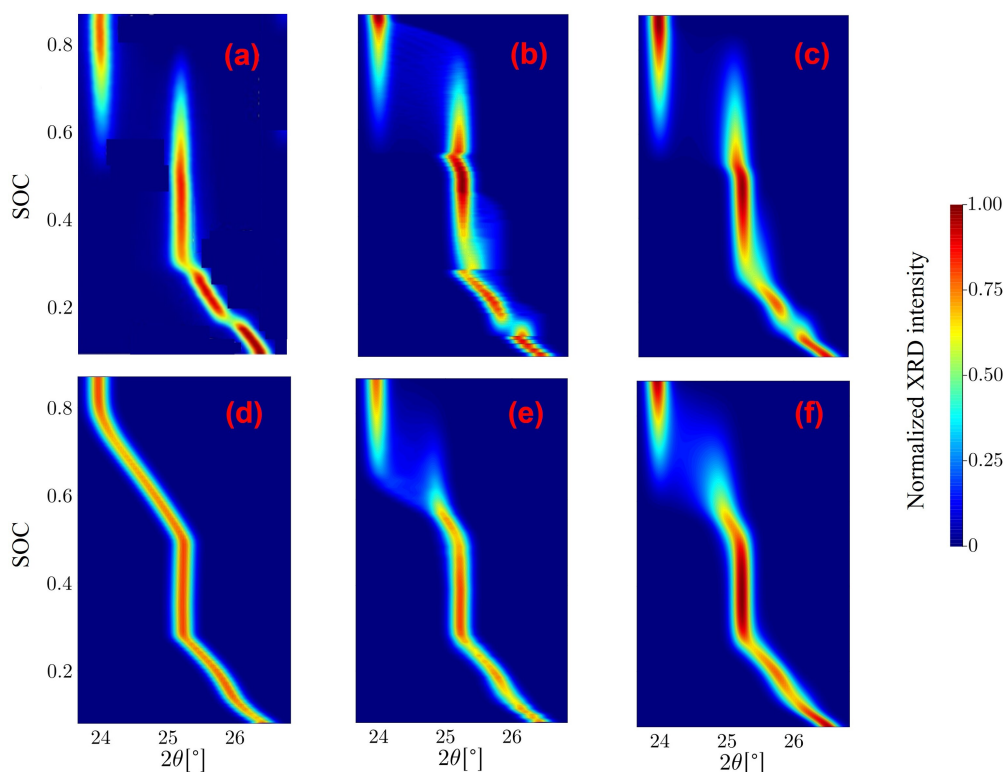
10

Figure 4: Contour plot of changes in the 2θ angle and intensity of graphite basal reflections for a graphite electrode undergoing a C/20 charge at 25 °C. (a) *Operando* XRD measurement [35]. (b) Simulated XRD using the phase-field Gibbs free energy model. The numerical results at certain SOCs may not be reliable due to large chemical potential gradients and sharp phase boundaries. (c) Simulated XRD using the reaction-limited Gibbs free energy model. (d) Simulated XRD using the PET-based free energy model. (e) Simulated XRD using an OCP-fitted Gibbs free energy model with the phase-field formulation. (f) Simulated XRD using an OCP-fitted Gibbs free energy model with the reaction-limited formulation.

intercalations and transport, causing the lithiation front to move and "shoulders" or stagnations in the filling fractions to form [9]. Such energy-barrier-related phenomena have been observed experimentally using *operando* XRD [9, 40], yet remain elusive in current modeling efforts.

The internal states of graphite are closely coupled with reaction kinetics and ionic transport, which together significantly influence its intercalation dynamics. Many degradation mechanisms in graphite draw side reaction currents from the intercalation currents, meaning they are also affected by these internal states. One unexpected feature observed during the heterogeneous delithiation of graphite is the increase in Stage 1 population at the end of a constant voltage discharge [9, 40]. Since this phenomenon occurs only in specific stages, it is of great value to quantify the contribution of each stage, specifically the mass fractions associated with them. Traditionally, decoupling the contributions of different stages is typically achieved through Rietveld refinement and integration of the XRD peaks. However, this technique can lead to ambiguous interpretations because XRD patterns may be obscured by peaks from the cathode, current collector, or casing. Additionally, some phases are challenging to decouple due to weak reflection

11

splitting of Bragg peaks [41]. In this context, our Gibbs energy models, combined with a suitable physics-based formulation, can help accurately quantify the dynamics of phase populations, thereby enhancing the predictive capability of both simulations and experiments.

The applications of realistic Gibbs free energy models featuring accurate energy barriers are essential for advancing the understanding and prediction of graphite internal intercalation dynamics. First, XRD simulations based on these models facilitate quantitative degradation modeling, which is key for developing health-conscious control strategies in battery management systems. For instance, accurately predicting the formation of LiC_6 phase in graphite is critical for optimizing fast charging protocols to limit lithium plating. Second, model-assisted Rietveld refinement, leveraging the detailed energy barrier information, can be used to interpret experimental XRD results more effectively. This approach can help decouple complex phase contributions that might be challenging in experimental data, leading to a more reliable analysis of the internal states and dynamics within the battery.

Commercial cells

For commercial cells, three-electrode experiments can be performed to characterize individual electrodes, as detailed in *Supporting Information* S1. Unlike in coin cells, the lithium-ion concentration in the electrolyte and the intercalation rate at the particle surface can generally be treated as constant along the in-plane direction. Under low current conditions, these quantities can also be considered uniform across the electrode thickness (out-of-plane) dimension (see *Supporting Information* S4.1). This simplification allows chemical potentials to be inferred without coupling electrolyte dynamics in the thickness dimension to intercalation dynamics, which would otherwise introduce additional PDEs and algebraic constraints. However, when currents exceed the limits of the single-particle assumption, electrolyte dynamics and spatially distributed intercalation rates must be incorporated for accurate modeling and predictions for downstream model-based applications.

To demonstrate the effectiveness of our approach in downstream applications, such as terminal voltage prediction, the inferred chemical potential is integrated into a full-cell model. This model uses a phase-field formulation for ion concentration in the solid phase, coupled with distributed ion concentration in the electrolyte and distributed intercalation rates, as previously formulated by Huang et al. [25]. The parameterization is based on a LG™ M50 cylindrical cell [38], with selected parameters adapted to cells used by Kirkaldy et al. [42] to account for cell-to-cell variation. Parameter identification is performed using C/2 constant-current discharge data of a pristine cell at 25 °C, implemented via a differential evolution optimizer. Model validation is carried out using hybrid pulse power
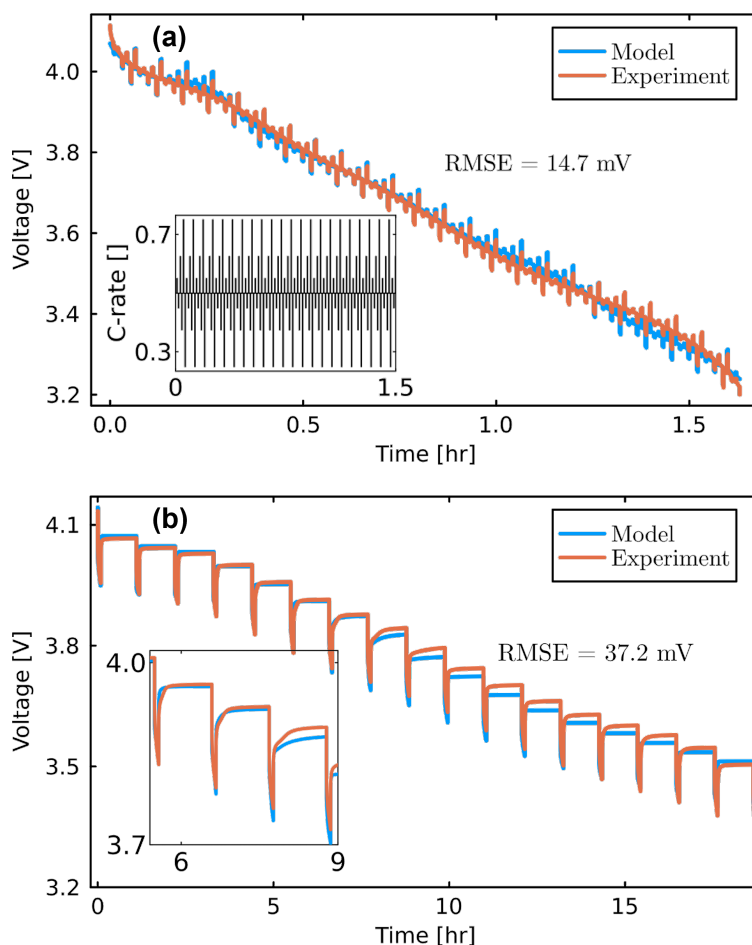
12

Figure 5: Testing of a full-cell model using two current profiles cooled at 25 °C. (a) Voltage prediction under an HPPC-type profile, with the inset showing the corresponding current profile. (b) Voltage prediction for a GITT profile, with the inset displaying an enlarged view of relaxation behavior on the voltage curve.

characterization (HPPC) and galvanostatic intermittent titration technique (GITT) profiles, which are widely used for evaluating battery performance and relaxation dynamics.

Fig. 5a shows the voltage prediction of the fitted full-cell model under an HPPC-type current profile, where the inset depicts the current profile used during testing. The prediction closely tracks the experimental data, achieving a root-mean-square error (RMSE) of 14.7 mV. In Fig. 5b, the voltage prediction for a GITT-type profile is shown to effectively capture the transient behavior of the voltage relaxation but exhibits a small steady-state error for certain GITT pulses. This highlights a persistent challenge in parameterizing full-cell electrochemical models, especially for pulsing and dynamic current profiles. We emphasize that, while many battery models with differing physical assumptions can achieve reasonable accuracy in terminal voltage prediction, faithful internal state estimation remains a significant advantage of more physically detailed models. Such insights are vital for applications like battery diagnostics and

13

health-aware control, where internal states are more informative than voltage alone.

Theory

Physics-based learning of hidden physics and uncertainties

Physics-based electrochemical models, typically formulated as PDEs or partial-differential algebraic equations (PDAEs), face significant challenges when applied to real-world energy storage systems. These challenges arise from two main factors. First, the high-dimensional parameter space inherent in these models complicates parameter identification, particularly when using Bayesian estimation techniques. Over-parametrization exacerbates this issue, leading to poor inferability, predictability, and generalizability due to the increased prediction uncertainty caused by fitting numerous free parameters. Second, all models are subject to modeling errors as a result of changed operating conditions, parameter variability, and simplifications made during model development. These errors are often introduced by mis-specifications in the dynamic system, which can result from unphysical assumptions or oversimplifications during model order reduction.

A major source of modeling errors arises from hidden physics that remain latent and unaccounted for in the model specification. Built on our prior work [25], BMINN is specifically designed to handle these errors while accounting for uncertainties in general dynamic systems. The architecture and key concepts of BMINN are illustrated in Fig. 6. This hybrid approach ensures fidelity to physical laws while leveraging the approximation capacity of neural networks and quantifying uncertainties given the available, potentially noisy data or incomplete data.

The interpretability of BMINN is attributed to its hybrid architecture, where known physics-based equations constrain the learning process and hidden states correspond to electrochemical states of a battery. The unknown components (Fig. 6d) characterizing the hidden physics, are explicitly parameterized and inferred. Furthermore, the Bayesian component of BMINN provides posterior distributions for learned parameters, offering a probabilistic measure of uncertainty. This uncertainty accounts for data noise, sparsity, and model mis-specification, making it a critical indicator of the reliability and robustness of predictions.

BMINN is achieved by significantly extending our previously proposed MINN that introduced neural networks to approximate part of PDAE-based physical models with a predefined model structure and without uncertainties. Specifi-
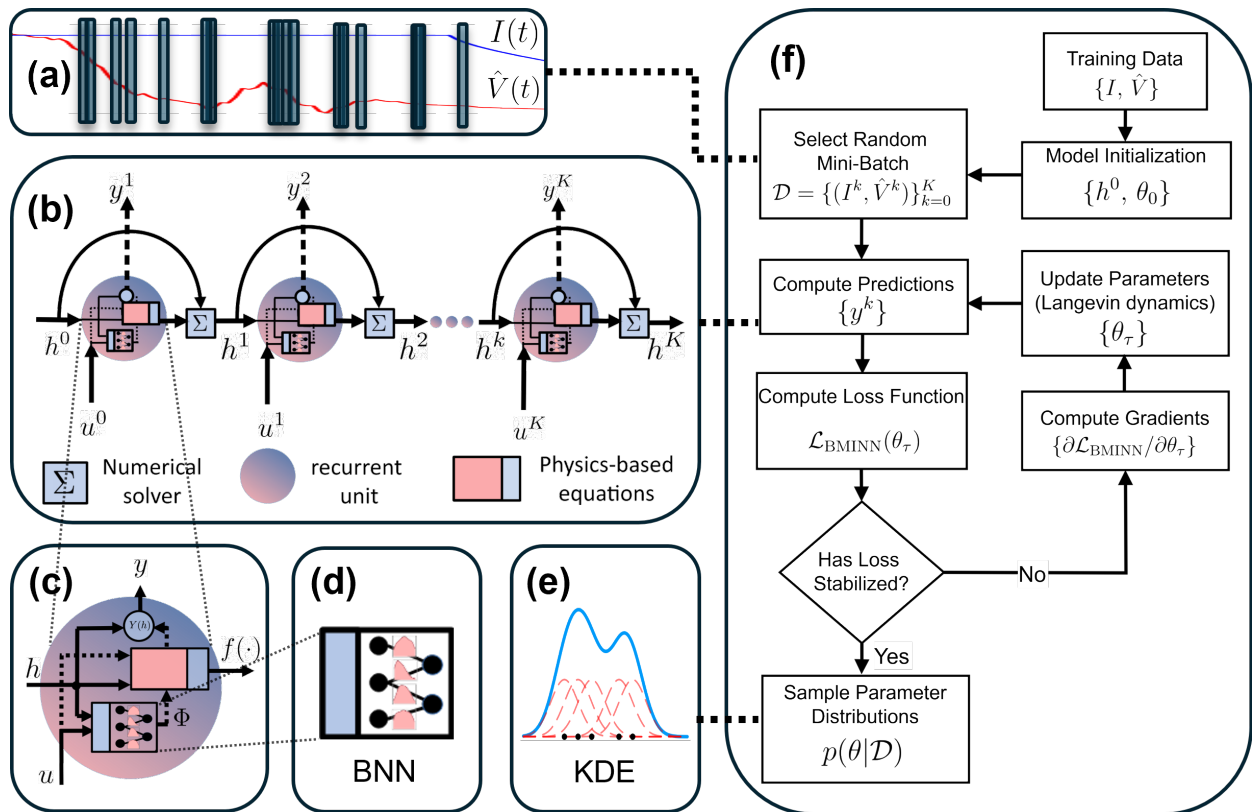
14

Figure 6: The architecture and key concepts of BMINN for learning hidden physics and quantifying uncertainties in dynamic systems. (a) Data batching illustrated for battery training data, consisting of a two-dimensional vector of K randomly selected points from current and voltage time-series data. (b) The iterative update process of hidden states h^k, input u^k, and output y^k in the BMINN architecture. (c) The design of the physics-based recurrent unit, incorporating physics-based equations, Bayesian neural networks (BNN), an output function $y = Y(h)$, and an unknown function Φ representing the hidden physics. (d) Quantification of uncertainties by learning the distributions of weights and biases in BNN. (e) Sampling of the posterior distribution using kernel density estimation (KDE). (f) Flowchart of the BMINN training algorithm illustrated for a battery system.

cally, BMINN targets a class of non-autonomous PDAE-based systems described by

$$\frac{\partial H_d}{\partial t} = F\left(t, H_d, H_z, \Phi(\cdot), u\right), \tag{1a}$$

$$0 = G\left(t, H_d, H_z, \Phi(\cdot), u\right), \tag{1b}$$

$$y = Y\left(t, H_d, H_z, \Phi(\cdot), u\right), \tag{1c}$$

where t is time, u denotes the external control input that makes the system non-autonomous, y is the measurable system output, and F, G, and Y are functions. H_d and H_z represent differential states and algebraic variables, respectively. All the states and algebraic variables are time-dependent and spatially distributed, in which the spatio-temporal coordinates, i.e., t and $\mathbf{x}$, are ignored for brevity. $\Phi(\cdot)$ is an unspecific function that can be dependent on t, $\mathbf{x}$, H_z H_d, or u., and it is included in the model formulation to cover any possible hidden physics and uncertainties. The identification of

15

$\Phi(\cdot)$ will be affected by the employed labeled input-output dataset, denoted by $\mathcal{D}$. By leveraging Bayesian principles to model uncertainty in data, Bayesian machine learning can be a powerful tool to identify $\Phi(\cdot)$. Because of modular and flexible design, recurrent neural networks (RNN) are particularly suited for sequence-to-sequence applications, while as a bi-directional network, residual neural networks (ResNets) can model dynamic systems with time-stepping of states governed by the system dynamics and control input. As demonstrated by the MINN framework [25], integrating these different neural networks can enable highly efficient learning for the dynamics of complicated systems that are nonlinear, non-autonomous, and singularly perturbed. Following this trend, we propose to approximate $\Phi(\cdot)$ by Bayesian neural network (BNN), Φ_{BNN}, parameterized by p_θ, leading to

$$\Phi(\cdot) = \Phi_{\mathrm{BNN}}\left(t, \mathbf{x}, H_d, H_z, u; p_\theta\right), \tag{2}$$

where p_θ stands for the distribution of parameters θ, namely $p_\theta = p(\theta)$, and θ includes both battery physical parameters and the BNN's parameters. Consequently, the formulation of BMINN can be given by

$$\frac{\partial H_d}{\partial t} = F\left(t, H_d, H_z, \Phi_{\mathrm{BNN}}, u\right), \tag{3a}$$

$$0 = G\left(t, H_d, H_z, \Phi_{\mathrm{BNN}}, u\right), \tag{3b}$$

$$y = Y\left(t, H_d, H_z, \Phi_{\mathrm{BNN}}, u\right). \tag{3c}$$

Note that the model formulation obtained above for BMINN blends the physics-based part captured by functions F, G, and Y, and the data-driven part, i.e., Φ_{BNN} within each of these functions.

By appropriately discretizing (3) in both the spatial and time domains, we can obtain BMINN in the discrete form

$$h_d^{k+1} = f\left(k, \delta t^k, h_d^k, h_z^k, \Phi_{\mathrm{BNN}}^k, u^k\right), \tag{4a}$$

$$0 = g\left(k, h_d^k, h_z^k, \Phi_{\mathrm{BNN}}^k, u^k\right), \tag{4b}$$

$$y^k = y\left(k, h_d^k, h_z^k, \Phi_{\mathrm{BNN}}^k, u^k\right), \tag{4c}$$

where k is the discrete-time index. δt^k is the step size at time step k that can be controlled by an adaptive time integrator. h_d and h_z are the spatially discretized differential states and algebraic variables, respectively, and $\Phi_{\mathrm{BNN}}^k = \Phi_{\mathrm{BNN}}(k, \mathbf{x}, h_d^k, h_z^k, u^k; p_\theta)$. The form of the function $f(\cdot)$ is dependent on the time integration scheme, which can take

16

the arguments h_d^{k+1} and h_z^{k+1} if an implicit scheme is used. Φ_{BNN}^k can be parameterized by BNN with a set of parameters and hyper-parameters to optimize.

The distribution p_θ of the parameters θ is learned by evaluating the loss function $\mathcal{L}_{\text{BMINN}}$ for multiple parameter sets sampled from p_θ

$$\mathcal{L}_{\text{BMINN}}(\theta) = \frac{1}{K} \sum_{k=0}^{K} \left[y\left(k, h_d^k, h_z^k, \Phi_{\text{BNN}}^k, u^k\right) - \hat{y}^k \right]^2 \delta t^k, \tag{5}$$

$$\text{s.t.} \quad (4a)-(4b),$$

where K denotes the total number of labelled input-output pairs, i.e. $\mathcal{D} = \{[u^1, \hat{y}^1], \cdots, [u^k, \hat{y}^k], \cdots, [u^K, \hat{y}^K]\}$, and $\hat{y}^k$ is the measured system output. If the value of $\mathcal{L}_{\text{BMINN}}$ for a sampled model is small, it implies that the parameter values produce model outputs closely matching the observed data. This means the loss function defined above for a sampled parameter set is inversely proportional to the likelihood of $\mathcal{D}$ for a given θ, denoted by $p(\mathcal{D}|\theta)$. Specifically, the relationship between the loss function and the log-likelihood $\log p(\mathcal{D}|\theta)$ is given by:

$$\mathcal{L}_{\text{BMINN}}(\theta) \propto -\log p(\mathcal{D}|\theta). \tag{6}$$

Uncertainty quantification

The BNN, Φ_{BNN}^k, in the general problem formulation of BMINN can be realized by a deep stochastic neural network consisting of an input layer $\mathbf{a}^{[1]}$, a succession of L layers, and an output layer polluted by random noise $\boldsymbol{\epsilon}$. This neural network can be generally formulated as

$$\begin{cases} \mathbf{a}^{[1]} = [k, \mathbf{x}, h_d^k, h_z^k, u^k]^T, \\ \mathbf{a}^{[l]} = \sigma\left(\mathbf{W}^l \mathbf{a}^{[l-1]} + \mathbf{b}^l\right), \quad \text{for} \quad l = 2, 3, ..., L, \\ \Phi_{\text{BNN}}^k = \mathbf{W}^L \mathbf{a}^{[L]} + \mathbf{b}^L + \boldsymbol{\epsilon}^k, \end{cases} \tag{7}$$

where $\sigma(\cdot)$ is the activation function. For layer l, $\mathbf{W}^l$, $\mathbf{b}^l$, and $\mathbf{a}^{[l]}$ represent the weight matrices, biases, and activation.

The parameters θ embedded in Φ_{BNN} are considered random variables for which the entire distribution is estimated from $\mathcal{D}$. Given a prior distribution of parameters $p(\theta)$, by Bayes' theorem, the posterior distribution $p(\theta|\mathcal{D})$ is proportional to the product between the prior and the likelihood of the dataset given the parameter $p(\mathcal{D}|\theta) = \Pi_1^K p([u^k, \hat{y}^k]|\theta)$,

17

i.e.,

$$p(\theta|\mathcal{D}) \propto p(\theta)p(\mathcal{D}|\theta). \tag{8}$$

The most probable parameter set of θ, defined as $\theta_{\max}$, in a MAP estimation, maximizes the posterior distribution. This is done by taking the logarithm of posterior in (8), leading to the maximization problem

$$\theta_{\max} = \arg\max_{\theta} \left[\log p(\mathcal{D}|\theta) + \log p(\theta)\right]. \tag{9}$$

To take advantage of the full posterior distribution, one has to evaluate multi-dimensional integrals, such as the posterior expectation and variance with respect to parameters θ, or to sample from the posterior using Markov chain Monte Carlo. However, this generally does not scale well with the number of parameters involved in physics-based machine learning. To avoid this, we adopt the stochastic gradient Langevin dynamics (SGLD) [43], which stochastically updates the parameters according to the Langevin stochastic differential equation:

$$\theta_{\tau+1} = \theta_\tau + \frac{\epsilon_\tau}{2}\left(-\frac{\partial\mathcal{L}_{\text{BMINN}}(\theta_\tau)}{\partial\theta_\tau} + \frac{\partial\log p(\theta_\tau)}{\partial\theta_\tau}\right) + \Gamma_\tau, \text{ where } \Gamma_\tau \sim \mathcal{N}(0, \epsilon_\tau) \tag{10}$$

where τ is the iteration index, ϵ_τ is a positive parameter denoting the learning rate, and Γ_τ is a normally distributed random variable in the Langevin dynamics to ensure that the parameter trajectory converges to a full posterior distribution. The loss term $\mathcal{L}_{\text{BMINN}}(\theta_\tau)$ defined in (5) is equivalent to the negative log-likelihood function due to (6). $\partial\log p(\theta_\tau)/\partial\theta_\tau$ serves as a regularization term in the above update law for parameters θ.

Learning chemical potentials

The BMINN framework facilitates accurate identification of hidden physics within PDE- or PDAE-based models, specified in *Supporting Information* S2–S4, along with their associated physical parameters. To learn material-specific chemical potentials in these physics-based formulations, we first acknowledge that the battery data consists of externally measurable quantities, such as the applied current I and voltage V, as well as internal states, such as the lithium-ion concentrations. While I and V can be readily obtained in a three-electrode setup, the internal states of electrodes must be estimated using advanced spectroscopy techniques. Among these, *operando* XRD spectroscopy has proven effective for capturing internal states under battery operational conditions [9]. However, such methods require access to high-energy synchrotrons and specialized cell designs. Furthermore, the X-ray or neutron exposure involved

18

in these techniques can inadvertently alter the system states, including the electrode potential and temperature [44], thereby impacting the reliability of the data for learning chemical potentials.
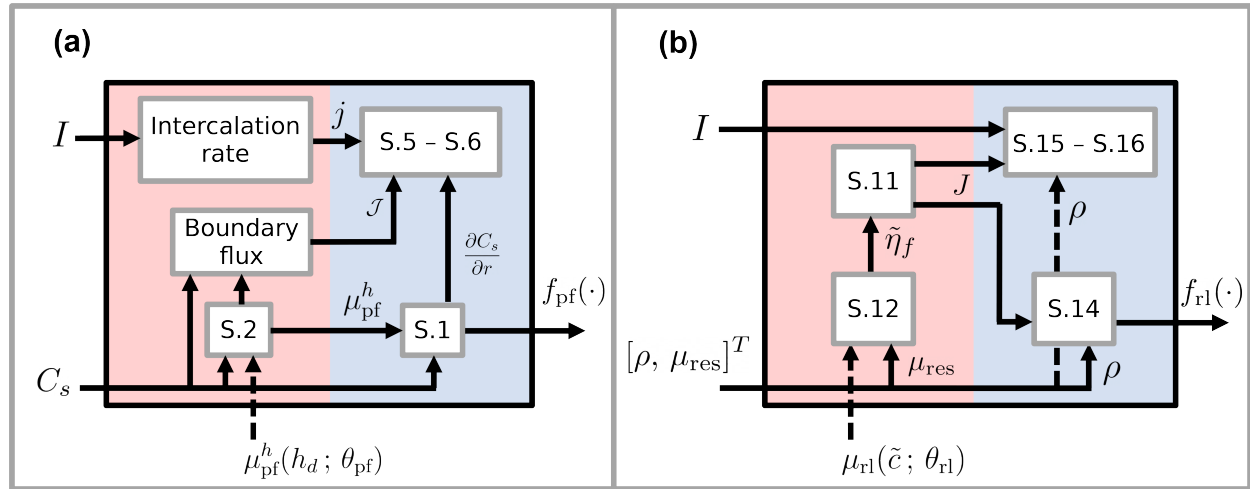

Figure 7: The physics-based recurrent unit design in BMINN for learning missing physics parameterized by u_{pf}^h and u_{rl}. (a) The recurrent unit within BMINN realized for the phase-field model with the hidden state $h_d = C_s$ and control input $u = I$. (b) The recurrent unit realized for the reaction-limited model with hidden state $[h_d, h_z]^T = [\rho, \mu_{res}]^T$ and control input $u = I$. The equations S.1–S.16 in the figure correspond to physics-based formulations laid out in *Supporting Information* S2–S3.

To infer chemical potentials from externally measured current-voltage data using BMINN, we design two physics-based recurrent units corresponding to the phase-field and reaction-limited models, as illustrated in Fig. 7. For the dynamic electrochemical system of graphite electrodes, the hidden states, h_d, represent lithium-ion concentrations in active materials, C_s, in the phase-field model, while in the reaction-limited model, the hidden states are $[h_d, h_z]^T = [\rho, \mu_{res}]^T$, where ρ and μ_{res} denote the population density and reservoir chemical potential, respectively. After spatial discretization, the dynamic part of the PDE system (S.1)–(S.7) and the PDAE system (S.11)–(S.16) in the *Supporting Information* are expressed in the following forms

$$\frac{dh_d}{dt} = f_{pf}\left(h_d, \mu_{pf}^h(h_d; \theta_{pf}), I(t)\right) \qquad \text{(phase-field model);} \qquad (11)$$

$$\frac{dh_d}{dt} = f_{rl}\left(h_d, \mu_{rl}(\tilde{c}; \theta_{rl}), h_z, I(t)\right) \quad \text{(reaction-limited model),} \qquad (12)$$

$$0 = g_{rl}\left(h_d, \mu_{rl}(\tilde{c}; \theta_{rl}), h_z, I(t)\right) \quad \text{(reaction-limited model);} \qquad (13)$$

Here, the system input is the applied current. The nonlinear functions f_{pf}, f_{rl} and g_{rl} describe the system dynamics, and the chemical potentials, μ_{pf}^h and μ_{rl}, associated with the phase-field and reaction-limited models, respectively, are learned alongside their physical parameters, θ_{pf} and θ_{rl}, during the training of BMINN. The nonlinear functions f_{pf} and f_{rl} correspond to the general function $f(\cdot)$ in (4a) and in the recurrent units shown in Fig. 6c, representing the

19

phase-field and reaction-limited cases, respectively. For PDAE formulations, the constraint $g_{rl} = 0$ is enforced by employing a DAE solver. To fully implement BMINN for the battery system, the loss function (5) is established with multiple parameter sets sampled from the distribution of θ_m, where $m \in \{pf, rl, pet\}$ represents the model indices for phase-field, reaction-limited, and PET-based models, respectively. The loss function for each model $\mathcal{L}_{\text{BMINN}}(\theta_m)$ is in the form

$$\mathcal{L}_{\text{BMINN}}(\theta_m) = \frac{1}{K} \sum_{k=0}^{K} \left(V_m^k - \hat{V}^k\right)^2, \tag{14}$$

where the battery dataset $\mathcal{D} = \{(I^k, \hat{V}^k)\}_{k=0}^{K}$ consists of measured system outputs $\hat{V}^k$ and simulated outputs V_m^k, and K denotes the number of samples in the randomly selected mini-batch. This loss function is subject to constraints imposed by the electrode dynamics, as defined in equations (11)–(13). The implementation to derive θ_m follows the Langevin stochastic differential equation (10), which provides uncertainty quantification for the learned parameters.

Discussion and outlook on model-based applications

Characterization of degradation

Fast-charging applications are limited by battery degradation [45–47]. The advantage of an accurate model for phase transition lies in its ability to characterize the shifting and scaling of the operating SOC range for each electrode during aging. The shifting and scaling are indicative of different degradation modes [48], and they can be subsequently used as features for lifetime and degradation prognostics [49]. Aging-adaptive modeling involves calibrations of stoichiometry parameters that rely on the fitting of a pseudo-open-circuit voltage curve. Even though this method can characterize the change in stoichiometry parameters corresponding to the maximum and minimum cutoff voltages, the predefined OCP functions limit the accuracy. The error can be large at the end of discharge, where the voltage is dominated by graphite anode potential at low capacity values. As a result, inaccurate identification of stoichiometry parameters will penalize any battery models.

Other characterization techniques for aging include terminal voltage-based differential voltage (DV) or incremental capacity (IC) analyses. These methods routinely require precise measurements at cell level. While voltage sensors are typically deployed for individual cells or parallel-connected units, the allocation of current sensors is often limited to one per battery pack, largely due to the prohibitive costs associated with sensors. This deficiency in accurate current data for cells in parallel poses a significant obstacle to the effective implementation of DV and IC analyses at cell

20

level as well as the development of methodologies reliant on DV and IC. Further, for a battery unit, module, or pack, battery voltage is always available but will inevitably suffer from measurement noise and potential drifts.

To address the above issues, the BMINN battery models offer a valuable solution. First, with material-specific chemical potentials and physical parameters learned from voltage measurements, the phase-field and reaction-limited battery models have demonstrated their ability to predict the anode potential accurately. As opposed to predefined OCP functions, the developed models feature thermodynamically consistent descriptions of phase transition. Second, our approach can be easily extended to other cathode materials to form a full-cell model. By leveraging the anode and cathode potentials predicted by our model, we can significantly improve the precision and reliability of DV and IC analyses. This improvement can be achieved through, e.g., an integration of measured data and model predictions using Kalman filters, thereby enhancing the accuracy and robustness of the overall analysis. Lastly, as the stoichiometry parameters undergo changes in aging, an associated phenomenon arises: the voltage curves between adjacent plateaus are smeared, resulting in the broadening of DV and IC peaks and troughs. This occurrence is attributed to side reactions unevenly taking place within the particle populations. Notably, existing methodologies have yet to model these effects due to their focus on terminal voltage, and inaccuracy in the internal state estimation. This gap may be effectively bridged by the two superior battery models resulting from BMINN.

For lifelong aging-adaptive modeling, one will need to re-parameterize all aging-related model parameters consistently during the battery lifetime. To track the parameters effectively over time, it is efficient to combine cloud-based model training and edge-based model deployment. Namely, BMINN is trained on the cloud periodically using current-voltage data that are measured locally and sent to the cloud. Then, the newly trained model parameters will be used to update the model in the local battery management system. This cloud-edge joint implementation depends on battery-powered devices, usage scenarios, communication protocols, sensors, and computing hardware, and should be tailored to fit individual applications.

Modeling electrochemical impedance

The electrochemical impedance of a battery is sensitive to the equilibrium behaviors of its half cells. This is because the reaction kinetics is calculated from the overpotential that is dependent on an accurate estimation of the electrode's equilibrium surface concentration. Other than the fitted OCP functions, the widely adopted method in modeling electrochemical impedance is the multi-site multi-reaction (MSMR) theory [28], which breaks the OCP curve up into regions of solid-solution slopes and two-phase plateaus. It assumes Ernest's relation within the sloping regions and

21

constant potential in the plateau regions. However, this model is parameterized using pseudo-OCP measurements, which deviate from true OCP due to polarization and hysteresis effects [33]. The proposed BMINN framework for battery modeling, on the other hand, offers a streamlined alternative for modeling the equilibrium behavior of electrodes. In particular, the reaction-limited model is known to capture not only the resistance polarization but also hysteresis effects at low current [34]. Battery models within the BMINN framework, leveraging the insights provided by physics-based models and cell-specific voltage data, can characterize the equilibrium behavior and enhance the accuracy of impedance modeling.

Mechanical models

It is well-known that the pressure change during cycling of graphite-based battery cells is dominated by their negative electrodes. The pressure or displacement measured using external sensors is due to the total dilation of polycrystalline volume expansion and contraction. This pressure, or displacement, can be quantified using external sensors. However, it is important to note that this measurement reflects the total volume change rather than the composition of changes associated with individual phase populations. Consequently, relying solely on pressure sensors is insufficient to characterize dynamic compositions of phases during operational conditions. In certain diagnostic techniques for detecting lithium plating, abnormal pressure changes are correlated with *post-mortem* optical evidence of plating occurrences [50]. For graphite, the phenomenon of plating typically manifests during the Stage 2 to Stage 1 transition, where a specific population of particles is transitioning from "half full" to "full", prompting a reduction of lithium ions to lithium metal. The developed battery model offers precise means of quantifying the population involved in the 2–1 transition. When coupled with mechanical battery models, it holds the potential to estimate specific phase transitions indicative of lithium plating, providing a foundation for future research.

Conclusion

Learning hidden physics and unknown parameters of PDE or PDAE-based non-autonomous systems remains a significant challenge for energy storage systems, especially in the presence of parameter uncertainties and measurement noise. In this study, we have proposed a physics-based learning framework, BMINN, to systematically bridge this gap. BMINN seamlessly integrates physics-based principles with data-driven methods to learn unmodeled components and their associated uncertainties within a class of non-autonomous dynamic systems. Unlike purely data-driven approaches that learn input-output relationships, BMINN incorporates physical parameters and physically interpretable

hidden states by design, allowing it to effectively learn hidden physics in the system dynamics. At the same time, it employs Bayesian inference to enable robust uncertainty quantification and probabilistic assessments of predictions. Consequently, the developed framework offers exceptional generalizability, physical interpretability, adaptability, and data efficiency, while significantly surpasses existing methods in terms of accuracy. Furthermore, BMINN is highly generic and can be readily applied to various dynamic systems, thereby advancing model-based applications.

The applicability of BMINN has been successfully demonstrated in the learning of electrode-specific chemical potentials and Gibbs free energies, which govern the driving force for phase transitions. Using readily available current-voltage data and two plausible formulations, BMINN learns thermodynamically consistent potentials and energies, capturing complex staging characteristics, energy barriers, and phase-separating dynamics that are elusive to conventional approaches. Compared to PET-based and OCP-fitted approaches, the learned chemical potentials provide a more detailed and accurate representation of the internal states that align closely with *operando* XRD results, including phase populations and energy barriers. These features are crucial for understanding fast-charging behaviors and degradation mechanisms, such as lithium plating and heterogeneous lithiation, which are challenging to observe experimentally. Furthermore, the integration of the learned chemical potentials into downstream applications, such as full-cell modeling, showcases its utility in battery modeling. The developed battery models can be used as powerful tools to advance battery design and management.

Acknowledgement

References

[1] J. Asenbauer, T. Eisenmann, M. Kuenzel, A. Kazzazi, Z. Chen, D. Bresser, The success story of graphite as a lithium-ion anode material – fundamentals, remaining challenges, and recent developments including silicon (oxide) composites, Sustainable Energy and Fuels 4 (2020) 5387–5416.

[2] D. Allart, M. Montaru, H. Gualous, Model of lithium intercalation into graphite by potentiometric analysis with equilibrium and entropy change curves of graphite electrode, Journal of The Electrochemical Society 165 (2) (2018) A380–A387.

[3] J. Li, X. Xu, Z. Luo, C. Zhang, Y. Zuo, T. Zhang, P. Tang, M. F. Infante-Carrió, J. Arbiol, J. Llorca, J. Liu, A. Cabot, Co-sn nanocrystalline solid solutions as anode materials in lithium-ion batteries with high pseudocapacitive contribution., ChemSusChem 127 (2019) 1451–1458.

[4] K.-H. Kim, W. Kim, S. Hong, Solid solution phosphide ($Mn_{1-x}Fe_xP$) as a tunable conversion/alloying hybrid anode for lithium-ion batteries, Nanoscale (2019).

[5] S. Jin, Y. Ye, Y. Niu, Y. Xu, H. Jin, J. Wang, Z. Sun, A. Cao, X. Wu, Y. dong Luo, H. Ji, L. Wan, Solid-solution based metal alloy phase for highly reversible lithium metal anode, Journal of the American Chemical Society 165 (2) (2020) 8818–8826.

[6] M. Heß, P. Novák, Shrinking annuli mechanism and stage-dependent rate capability of thin-layer graphite electrodes for lithium-ion batteries, Electrochimica Acta 106 (2013) 149–158.

[7] W. Rüdorff, U. Hofmann, über graphitsalze, Zeitschrift für Anorganische Allgemeine Chemie 238 (1938) 1–50.

[8] N. Daumas, A. Herold, Relations between phase concept and reaction mechanics in graphite insertion compounds, Comptes Rendus Hebdomadaires Des Seances De L Academie Des Sciences Serie C 268 (5) (1969) 373.

[9] D. P. Finegan, A. H. Quinn, D. S. Wragg, A. M. Colclasure, X. Lu, C. Tan, T. M. M. Heenan, R. Jervis, D. J. L. Brett, S. Das, T. Gao, D. A. Cogswell, M. Z. Bazant, M. D. Michiel, S. Checchia, P. R. Shearing, K. A. Smith, Spatial dynamics of lithiation and lithium plating during high-rate operation of graphite electrodes, Energy & Environmental Science (2020).

[10] M. Z. Bazant, Theory of chemical kinetics and charge transfer based on nonequilibrium thermodynamics, Accounts of Chemical Research 46 (5) (2012) 1144–1160.

[11] N. J. J. de Klerk, A. Vasileiadis, R. B. Smith, M. Z. Bazant, M. Wagemaker, Explaining key properties of lithiation in TiO_2-anatase li-ion battery electrodes using phase-field modeling, Physical Review Materials 1 (2017) 025404.

[12] R. B. Smith, E. Khoo, M. Z. Bazant, Intercalation kinetics in multiphase-layered materials, Journal of Physical Chemistry C 121 (2017) 12505–12523.

[13] M. Chandesris, D. Caliste, D. Jamet, P. Pochet, Thermodynamics and related kinetics of staging in intercalation compounds, The Journal of Physical Chemistry C (2019).

[14] M. Rykner, M. Chandesris, Free energy model for lithium intercalation in graphite: Focusing on the coupling with graphene stacking sequence, The Journal of Physical Chemistry C 126 (12) (2022) 5457–5472.

[15] X. Lu, M. Lagnoni, A. Bertei, S. Das, R. E. Owen, Q. Li, K. B. O'Regan, A. Wade, D. P. Finegan, E. Kendrick, M. Z. Bazant, D. J. L. Brett, P. R. Shearing, Multiscale dynamics of charging and plating in graphite electrodes coupling operando microscopy and phase-field modelling, Nature Communications 14 (2023).

[16] Y. Guo, R. B. Smith, Z. Yu, D. K. Efetov, J. Wang, P. Kim, M. Z. Bazant, L. E. Brus, Li intercalation into graphite: Direct optical imaging and Cahn-Hilliard reaction dynamics., The Journal of Physical Chemistry Letters 7 (11) (2016) 2151–2156.

[17] R. B. Smith, M. Z. Bazant, Multiphase porous electrode theory, Journal of The Electrochemical Society 164 (11) (2017) E3291.

[18] Y. Li, F. E. Gabaly, T. R. Ferguson, R. B. Smith, N. C. Bartelt, J. D. Sugar, K. R. Fenton, D. A. Cogswell, A. L. D. Kilcoyne, T. Tyliszczak, M. Z. Bazant, W. C. Chueh, Current-induced transition from particle-by-particle to concurrent intercalation in phase-separating battery electrodes., Nature Materials 13 (12) (2014) 1149–1156.

[19] J. Park, H. Zhao, S. D. Kang, K. Lim, C.-C. Chen, Y.-S. Yu, R. D. Braatz, D. A. Shapiro, J. Hong, M. F. Toney, M. Z. Bazant, W. C. Chueh, Fictitious phase separation in li layered oxides driven by electro-autocatalysis, Nature Materials 20 (2021) 991–999.

[20] M. Z. Bazant, Thermodynamic stability of driven open systems and control of phase separation by electro-autocatalysis., Faraday Discussions 199 (2017) 423–463.

[21] H. Zhao, M. Z. Bazant, Population dynamics of driven autocatalytic reactive mixtures, Physical Review E 100 (2019) 012144.

[22] D. Fraggedakis, N. Nadkarni, T. Gao, T. Zhou, Y. Zhang, Y. Han, R. M. Stephens, Y. Shao-horn, M. Z. Bazant, A scaling law to determine phase morphologies during ion intercalation, Energy & Environmental Science (2020).

[23] W. Dreyer, C. Guhlke, R. Huth, The behavior of a many-particle electrode in a lithium-ion battery, Physica D: Nonlinear Phenomena 240

24

(2011) 1008–1019.

[24] D. P. Finegan, J. Zhu, X. Feng, M. Keyser, M. Ulmefors, W. Li, M. Z. Bazant, S. J. Cooper, The application of data-driven methods and physics-based learning for improving battery safety, Joule 5 (2021) 316–329.

[25] Y. Huang, C. Zou, Y. Li, T. Wik, MINN: Learning the dynamics of differential-algebraic equations and application to battery modeling, IEEE Transactions on Pattern Analysis and Machine Intelligence 46 (12) (2024) 11331–11344.

[26] S. L. Brunton, J. L. Proctor, J. N. Kutz, Discovering governing equations from data by sparse identification of nonlinear dynamical systems, Proceedings of the National Academy of Sciences 113 (2015) 3932–3937.

[27] M. Raissi, P. Perdikaris, G. E. Karniadakis, Physics informed deep learning (Part II): Data-driven discovery of nonlinear partial differential equations, ArXiv (2017).

[28] M. W. Verbrugge, B. Koch, Modeling lithium intercalation of single-fiber carbon microelectrodes, Journal of The Electrochemical Society 143 (1996) 600–608.

[29] K. E. Thomas-alyea, C. Jung, R. B. Smith, M. Z. Bazant, In situ observation and mathematical modeling of lithium distribution within graphite, Journal of The Electrochemical Society 164 (2017).

[30] T. Gao, Y. Han, D. Fraggedakis, S. Das, T. Zhou, C.-N. Yeh, S. Xu, W. C. Chueh, J. Li, M. Z. Bazant, Interplay of lithium intercalation and plating on a single graphite particle, Joule (2021).

[31] H. Lian, M. Z. Bazant, Modeling lithium plating onset on porous graphite electrodes under fast charging with hierarchical multiphase porous electrode theory, Journal of The Electrochemical Society (2024).

[32] M. Doyle, T. F. Fuller, J. Newman, Modeling of galvanostatic charge and discharge of the lithium/polymer/insertion cell, Journal of The Electrochemical Society 140 (6) (1993) 1526–1533.

[33] A. V. der Ven, K. A. See, L. Pilon, Hysteresis in electrochemical systems, Battery Energy 1 (2022).

[34] W. Dreyer, J. Jamnik, C. Guhlke, R. Huth, J. Moškon, M. Gaberšček, The thermodynamic origin of hysteresis in insertion batteries., Nature materials 95 (2010) 448–53.

[35] C. Schmitt, A. Kube, N. Wagner, K. A. Friedrich, Understanding the influence of temperature on phase evolution during lithium-graphite (de-)intercalation processes: An operando X-ray diffraction study, ChemElectroChem (2021).

[36] N. Li, D. Su, In-situ structural characterizations of electrochemical intercalation of graphite compounds, Carbon Energy (2019).

[37] J. S. Edge, S. E. J. O'Kane, R. Prosser, N. Kirkaldy, A. N. Patel, A. Hales, A. Ghosh, W. Ai, J. Chen, J. Yang, S. Li, M.-C. Pang, L. B. Diaz, A. Tomaszewska, M. W. Marzook, K. Radhakrishnan, H. Wang, Y. Patel, B. Wu, G. J. Offer, Lithium ion battery degradation: what you need to know, Physical chemistry chemical physics : PCCP 23 (14) (2021) 8200–8221.

[38] C.-H. Chen, F. B. Planella, K. B. O'Regan, D. Gastol, W. D. Widanage, E. Kendrick, Development of experimental techniques for parameterization of multi-scale lithium-ion battery models, Journal of The Electrochemical Society (2020).

[39] G. Galuppini, M. D. Berliner, D. A. Cogswell, D. H. Zhuang, M. Z. Bazant, R. D. Braatz, Nonlinear identifiability analysis of multiphase porous electrode theory-based battery models: A lithium iron phosphate case study, Journal of Power Sources (2023).

[40] A. P. Monasterial, P. J. Weddle, K. Atkinson, D. S. Wragg, A. M. Colclasure, F. L. E. Usseglio-Viretta, N. Seitzman, J. S. Park, J. D. Almer, K. A. Smith, D. P. Finegan, Dynamic in-plane heterogeneous and inverted response of graphite to fast charging and discharging conditions in lithium-ion pouch cells, Small Science 3 (2023).

[41] A. Senyshyn, O. Dolotko, M. J. Mühlbauer, K. Nikolowski, H. Fuess, H. Ehrenberg, Lithium intercalation into graphitic carbons revisited: Experimental evidence for twisted bilayer behavior, Journal of The Electrochemical Society 160 (2013) 3198.

[42] N. Kirkaldy, M. A. Samieian, G. J. Offer, M. Marinescu, Y. Patel, Lithium-ion battery degradation: Comprehensive cycle ageing data and analysis for commercial 21700 cells, Journal of Power Sources 603 (2024) 234185.

25

[43] M. Welling, Y. W. Teh, Bayesian learning via stochastic gradient langevin dynamics, in: International Conference on Machine Learning, 2011.

[44] A. Klein, M. Sadd, N. Mozhzhukhina, M. Olsson, L. Broche, S. Xiong, A. Matic, Identifying the role of electrolyte additives for lithium plating on graphite electrode by operando x-ray tomography, Batteries & Supercaps 7 (7) (2024) e202400070.

[45] N. Guo, S. Chen, J. Tao, Y. Liu, J. Wan, X. Li, Semi-supervised learning for explainable few-shot battery lifetime prediction, Joule 8 (6) (2024) 1820–1836.

[46] S. Zhao, S. Chen, J. Zhou, C. Li, T. Tang, S. J. Harris, Y. Liu, J. Wan, X. Li, Potential to transform words to watts with large language models in battery research, Cell Reports Physical Science 5 (3) (2024) 101844.

[47] T. Lu, X. Zhai, S. Chen, Y. Liu, J. Wan, G. Liu, X. Li, Robust battery lifetime prediction with noisy measurements via total-least-squares regression, Integration 96 (2024) 102136.

[48] C. R. Birkl, M. R. Roberts, E. McTurk, P. G. Bruce, D. A. Howey, Degradation diagnostics for lithium ion cells, Journal of Power Sources 341 (2017) 373–386.

[49] Y. Zhang, T. Wik, J. Bergström, C. Zou, Machine learning-based lifelong estimation of lithium plating potential: A path to health-aware fastest battery charging, Energy Storage Materials (2024).

[50] C. Fang, B. Lu, G. Pawar, M. Zhang, D. Cheng, S. Chen, M. Ceja, J.-M. Doux, H. Musrock, M. Cai, B. Liaw, Y. S. Meng, Pressure-tailored lithium deposition and dissolution in lithium metal batteries, Nature Energy 6 (10) (2021) 987–994.

26